ADVANCED ELECTRONIC MATERIALS Open Access
www.advelectronicmat.de

Check for updates

Characteristics of $MAPbI_3$ Stacked on the GaN Nanowires-On-Glass

*Kwang Jae Lee, Yeong Jae Kim, Jung-Hong Min, Chun Hong Kang, Ram Chandra Subedi, Huafan Zhang, Latifah Al-Maghrabi, Kwangwook Park, Dante Ahn, Yusin Pak, Tien Khee Ng, Young Min Song, Boon S. Ooi, Osman M. Bakr, and Jungwook Min**

When implementing optoelectronic devices through the stacking of heterogeneous materials, considering the bandgap offset is crucial for achieving efficient carrier dynamics. In this study, the bandgap offset characteristics are investigated when *n*-type gallium nitride nanowires (*n*-GaN NWs) are used as electron transport layers in methylammonium lead iodide ($MAPbI_3$)-based optoelectronic devices. *n*-GaN NWs are grown on indium-tin-oxide (ITO)-coated glass via the plasma-assisted molecular beam epitaxy (PA-MBE) process to form the "GaN NWs-on-glass" platform. A $MAPbI_3$ thin film is then spin-coated on the GaN NWs-on-glass. X-ray photoelectron spectroscopy (XPS) shows that the valence and conduction band offsets in the $MAPbI_3$/*n*-GaN heterostructure are 2.19 and 0.40 eV, respectively, indicating a type-II band alignment ideal for optoelectronic applications. Prototype photovoltaic devices stacking perovskite on GaN NWs-on-glass show excellent interfacial charge-transfer ability, photon recycling, and carrier extraction efficiency. As a pioneering step in exploiting the diverse potential of the GaN-on-glass, it is demonstrated that the junction characteristics of $MAPbI_3$/*n*-GaN NW heterostructures can lead to a variety of optoelectronic device applications.

1. Introduction

Group III-nitride compound semiconductors, such as gallium nitride (GaN), indium nitride (InN), aluminum nitride (AlN), and their alloys ($Al_xGa_yIn_{1-x-y}N$), are pivotal in optoelectronics due to their wavelength tunability from ultraviolet (UV) to near-infrared (NIR).[1] Notably, *n*-type GaN is distinguished by its high conductivity and transparency, with over 85% transmittance across all visible wavelengths, facilitated by a straightforward silicon-doping process. GaN also supports diverse quantum structures, including quantum wells, nanowires, and quantum dots. Recently, the introduction of the GaN-on-glass platform, which enables growth on non-specific substrates, has drawn significant interest.[2] However, research related to the device application of GaN-on-glass is rarely reported, so further research must be undertaken.

Additionally, metal halide perovskites with the general formula AMX_3 (where A = $CH_3NH_3^+$, $CH(NH_2)_2^+$, Cs^+; M = Pb_2^+, Sn_2^+; X = I^-, Br^-, Cl^-) are emerging as leading materials in photovoltaics, light-emitting diodes, memory devices, and radiation detection due to their excellent properties and performance.[3] Nonetheless, the doping process to produce minority carriers remains a challenge in perovskite materials, underscoring the importance of integrating suitable electron/hole

K. J. Lee, O. M. Bakr
KAUST Catalyst Center (KCC)
King Abdullah University of Science and Technology (KAUST)
Thuwal 23955-6900, Kingdom of Saudi Arabia

Y. J. Kim, Y. M. Song
School of Electrical Engineering and Computer Science
Gwangju Institute of Science and Technology
Gwangju 61005, Republic of Korea

Y. J. Kim
Ceramic Total Solution Center
Korea Institute of Ceramic Engineering and Technology
Icheon 17303, Republic of Korea

The ORCID identification number(s) for the author(s) of this article can be found under https://doi.org/10.1002/aelm.202400095

© 2024 The Authors. Advanced Electronic Materials published by Wiley-VCH GmbH. This is an open access article under the terms of the Creative Commons Attribution License, which permits use, distribution and reproduction in any medium, provided the original work is properly cited.

DOI: 10.1002/aelm.202400095

J.-H. Min, C. H. Kang, R. C. Subedi, H. Zhang, L. Al-Maghrabi, T. K. Ng, B. S. Ooi, J. Min
Photonics Laboratory
King Abdullah University of Science and Technology (KAUST)
Thuwal 23955-6900, Kingdom of Saudi Arabia
E-mail: jungwook.min@kumoh.ac.kr

K. Park
Division of Advanced Materials Engineering
Division of Electronics and Information Engineering
Hydrogen and Fuel Cell Research Center
Jeonbuk National University
Jeonju 54896, Republic of Korea

D. Ahn, Y. Pak
Sensor System Research Center (SSRC)
Korea Institute of Science and Technology (KIST)
Seoul 02792, Republic of Korea

J. Min
Department of Optical Engineering
Kumoh National Institute of Technology
Gumi 39253, Republic of Korea

transport layers in the device structure. In perovskite solar cell cathodes, an electron transport layer (ETL) should not only extracts photocurrent but also possess various material properties such as chemical durability, interfacial properties, thermal/electrical conductivity, bandgap alignment, and optical properties (e.g., refractive index and transmittance). TiO_2, ZnO, SnO_2, $SrSnO_3$, and PCBM are well-known starting materials for the cathode structure. However, these wide bandgap oxide materials have several disadvantages, including low electron mobility, chemical instability in acid/base solutions, reactivity with the perovskite layer, high temperature processing, and difficulty in band tunability.[3b]

The concept of III-nitride/perovskite heterostructures using $Al_xGa_yIn_{1-x-y}N$ as electron/hole transfer layers has been extensively studied to advanced optoelectronic devices (Table S1, Supporting Information). To understand the interaction between GaN and perovskite materials thoroughly, band offset parameters have been explored using X-ray photoelectron spectroscopy (XPS). The investigation of band offsets, along with junction types, is vital as these parameters play a critical role in designing semiconductor heterostructures. They help determine the energy barriers essential for understanding electron and hole transport in device operation (Table S1, Supporting Information). In the literature, parameters such as valence band offset (VBO, ΔE_V) and conduction band offset (CBO, ΔE_C) have been measured or estimated, indicating their junction types. Examples include *n*-GaN/$MAPbBr_3$ (0.13±0.08 eV, 1.39±0.12 eV) with a type-I junction,[4] *n*-GaN/$MAPb_{3-x}Cl_x$ (2.15 eV, 0.35 eV) with a type-II junction,[5] *n*-GaN/$FA_{0.85}$-$MA_{0.15}Pb(I_{0.85}Br_{0.15})_3$ (1.67 eV, 0.49 eV) with a type-I junction,[6] *n*-GaN/single-crystal $CsPbBr_3$ (1.2 eV, 0.2 eV) with a type-II junction,[7] and *p*-GaN/$CsPbBr_3$ (1.95 eV, 0.18 eV) with a type-III junction.[8]

While significant efforts have been made, the exploration of band offset parameters, specifically VBO and CBO, in GaN/methylammonium lead iodide ($MAPbI_3$) heterostructures through XPS analysis remains relatively unexplored. Although GaN/$MAPbI_3$ heterostructures have been applied in optoelectronic devices, detailed reports on their band offset parameters are scarce. For example, in the case of $MAPbI_3$ perovskite photodetectors, planar *p*-GaN layers have been used as hole transport layers (HTLs), either by spray-coating[9] onto *p*-GaN templates or pressing *p*-GaN against spin-coated $MAPbI_3$.[10] Besides, perovskite solar cells (PSCs) have been constructed by spin-coating $MAPbI_3$ onto nanoporous *n*-GaN, which serves as an ETL.[3b] The integration of nanoporous GaN/GaN distributed Bragg reflector stacks has also been explored, with $MAPbI_3$ perovskite acting as the gain medium, in vertical-cavity surface-emitting lasers.[11]

Despite various research achievements and potential, there are still challenging issues in applying GaN to the perovskite research area. The high temperatures required for growing single- or poly-crystalline GaN make it impractical to grow or coat GaN on perovskite materials. Moreover, the use of single-crystalline substrates is crucial for GaN growth, complicating the use of GaN/perovskite heterostructures for optoelectronic applications due to the strong insulating properties of sapphire substrates and the opacity of silicon substrates to visible light.

In this study, we explored the bandgap alignment characteristics of *n*-GaN nanowires (NWs), used as the ETL, combined with $MAPbI_3$ serving as the active layer, to evaluate their potential in optoelectronic devices. The $MAPbI_3$ perovskite was spin-coated onto *n*-GaN NWs that were epitaxially grown on indium-tin-oxide (ITO)-coated glass substrates, known as the GaN-on-glass platform. We examined the structural properties of the heterostructure using cross-sectional high-resolution transmission electron microscopy (HRTEM) and analyzed the band offset parameters and heterojunction type through XPS. We observed enhancements in carrier extraction and photon recycling confirmed by photoluminescence (PL) measurements and finite-difference time-domain (FDTD) simulations. Moreover, we also confirmed that the GaN-on-glass has excellent junction characteristics with $MAPbI_3$ perovskite demonstrating device applicability. We fabricated prototype device structures using *n*-GaN NWs as an ETL in $MAPbI_3$ perovskite solar cells and photodetectors, indicating that the optimization of the heterogeneous integration of $MAPbI_3$/*n*-GaN and the understanding of their band offsets could support the development of functional prototypes for electronic and optoelectronic devices.

2. Results and Discussion

2.1. Band Alignment of $MAPbI_3$/GaN Heterostructure

To investigate the band alignment at the *n*-GaN and $MAPbI_3$ heterojunction as depicted in **Figure 1a**, we conducted high-resolution XPS measurements to determine the VBO at the interface. The evaluation of VBO at the *n*-GaN/$MAPbI_3$ heterostructure involved calculating the energy difference between the Ga $2p_{3/2}$ and Pb $4f_{7/2}$ core levels in the *n*-GaN/$MAPbI_3$ heterostructure and the energies of Ga$2p_{3/2}$ and Pb $4f_{7/2}$ core levels relative to the respective valence band maximum (VBM) of the *n*-GaN and $MAPbI_3$ samples. The VBO (ΔE_v) for the *n*-GaN/$MAPbI_3$ heterostructure can be calculated using the method proposed by Kraut et al.,[12] which is expressed as

$$\Delta\ E_V = \left(E^A_{\mathrm{Core}} - E^A_{\mathrm{VBM}}\right)_{MAPbI_3} - \left(E^B_{\mathrm{Core}} - E^B_{\mathrm{VBM}}\right)_{n-GaN} + \left(E^B_{\mathrm{Core}} - E^A_{\mathrm{Core}}\right)_{Heterostructure} \quad (1)$$

where $MAPbI_3$ and *n*-GaN are denoted as material *A* and *B*, respectively. The binding energies and VBM values were determined using XPS measurements as detailed in Section S1 (Supporting Information). The survey spectra presented in Figure S1 (Supporting Information), helped calculate the VBO and CBO values at 2.19 and 0.40 eV, respectively. A schematic band alignment diagram illustrating these offsets is shown in Figure 1b. The XPS results indicate a type-II band alignment, suitable for the *n*-GaN/$MAPbI_3$ heterostructure in perovskite solar cells and *n*–*i*–*p* photodetectors. Figure 1c displays an energy band diagram for these *n*-GaN/perovskite heterostructure devices.

2.2. Growth of GaN Nanowires on ITO-Coated Glass

In this section, we elaborate on fabricating a high-quality GaN-on-glass platform. **Figure 2a** presents a growth diagram for the self-assembled growth of Si-doped *n*-GaN NWs and a wetting layer on ITO-coated glass (GaN NWs-on-glass). The growth temperature is capped at 700 °C to prevent damage to the ITO interlayer (Figure S2, Supporting Information).[2b] The diagram

© 2024 The Authors. Advanced Electronic Materials published by Wiley-VCH GmbH

2199160x, 0, Downloaded from https://onlinelibrary.wiley.com/doi/10.1002/aelm.202400095 by Kumoh National Institute, Wiley Online Library on [12/07/2024]. See the Terms and Conditions (https://onlinelibrary.wiley.com/terms-and-conditions) on Wiley Online Library for rules of use; OA articles are governed by the applicable Creative Commons License

2199160x, 0, Downloaded from https://onlinelibrary.wiley.com/doi/10.1002/aelm.202400095 by Kumoh National Institute, Wiley Online Library on [12/07/2024]. See the Terms and Conditions (https://onlinelibrary.wiley.com/terms-and-conditions) on Wiley Online Library for rules of use; OA articles are governed by the applicable Creative Commons License

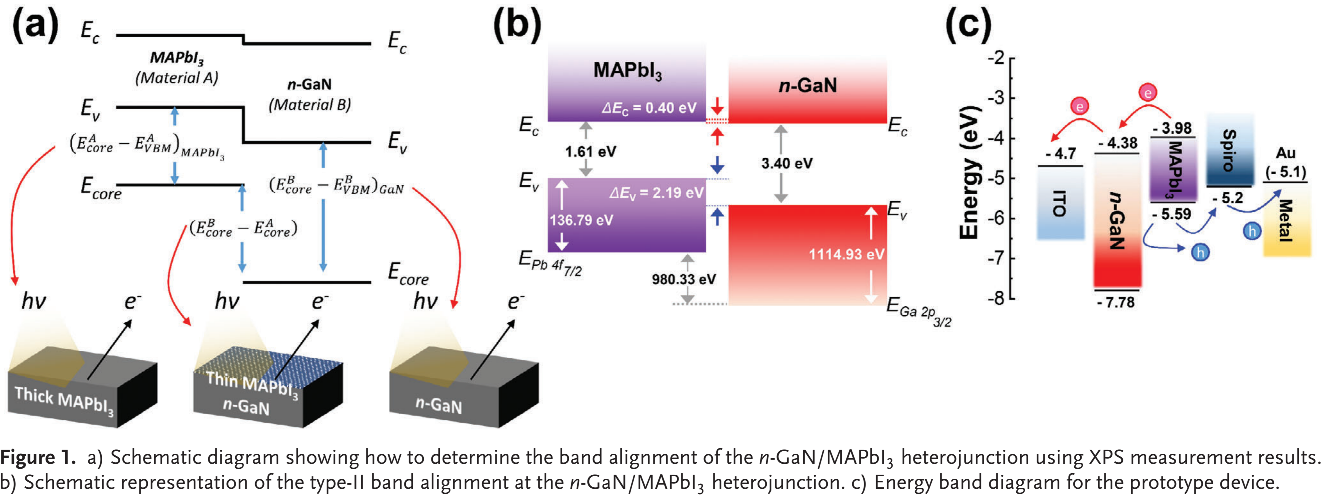

Figure 1. a) Schematic diagram showing how to determine the band alignment of the n-GaN/$MAPbI_3$ heterojunction using XPS measurement results. b) Schematic representation of the type-II band alignment at the n-GaN/$MAPbI_3$ heterojunction. c) Energy band diagram for the prototype device.

highlights two separate growth conditions for the n-GaN wetting layer (left) and the NWs (right).[13] Initially, the n-GaN wetting layer is grown at a relatively lower temperature (T_g = 500 °C) to encourage 3D nucleation.[14] The scanning electron microscopy (SEM) images on the bottom left depict a 70 nm-thick n-GaN wetting layer with a 3D morphology that covers each ITO columnar grain.[15] The inset displays an in situ reflection high-energy electron diffraction (RHEED) pattern along the <11–20> azimuthal direction, indicating a well-nucleated polycrystalline structure with its continuous ring pattern.[16] Following this, n-GaN NWs are grown at a higher temperature (T_g = 700 °C), promoting elongation, as confirmed by the SEM images on the bottom right.[17] The RHEED pattern inset shows oval shapes arranged as discrete ring patterns, indicating well-grown and fully elongated NWs (Section S2 and Figure S3, Supporting Information).[18] The optical image in Figure 2b shows the core part of the 2-inch GaN NWs-on-glass covered uniformly by n-GaN, with a sheet resistance of 65 $\Omega\cdot sq^{-1}$, demonstrating both conductivity and transparency. Transmittance and crystalline quality were compared by measuring UV–vis–NIR transmittance and PL spectra

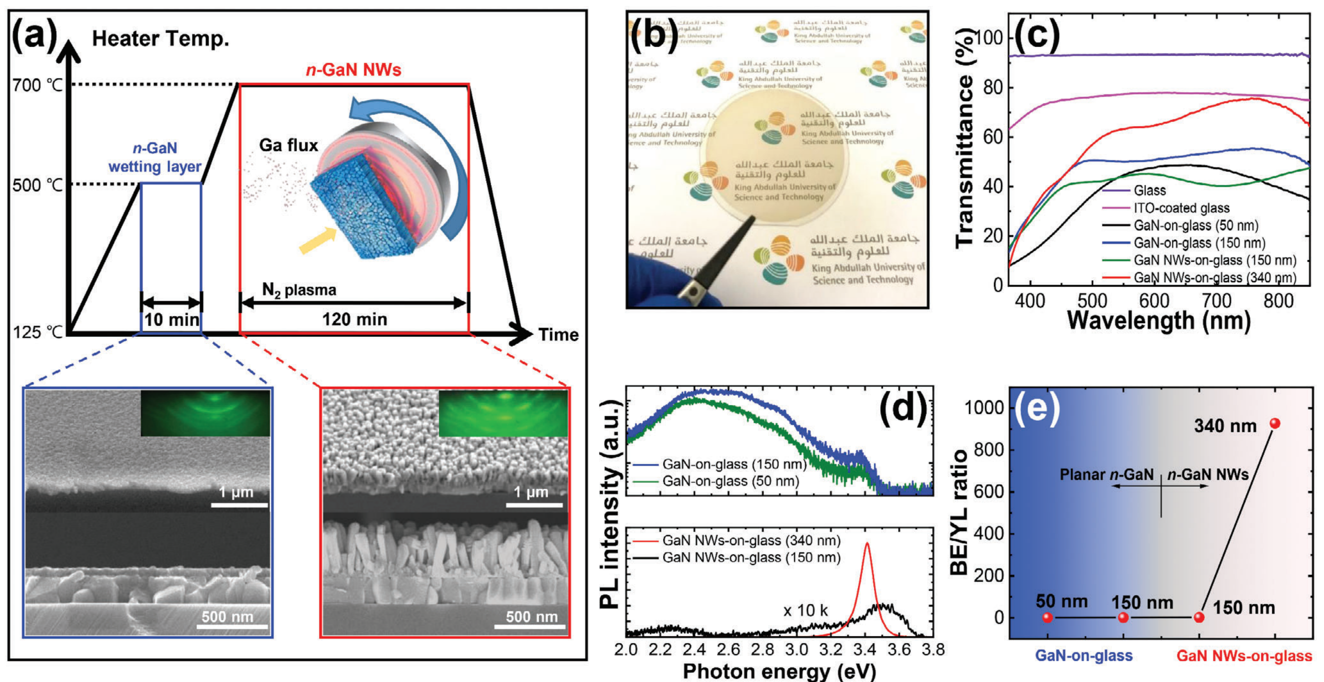

Figure 2. a) Temperature-time profile for the PA-MBE growth of the n-GaN wetting layer and NWs, including tilted and cross-sectional SEM images of the n-GaN wetting layer (bottom left) and n-GaN NWs (bottom right), respectively. Insets display in situ RHEED patterns during PA-MBE growth. b) Optical image of a 2-inch GaN NWs-on-glass. c) Comparison of light transmittance for bare glass, ITO-coated glass, and n-GaN nanostructures of various thicknesses. d) Room-temperature PL comparison across different thicknesses of GaN-on-glass and GaN NWs-on-glass samples. e) Comparison of BE/YL intensity ratios from the PL spectra of each sample.

© 2024 The Authors. Advanced Electronic Materials published by Wiley-VCH GmbH

2199160x, 0, Downloaded from https://onlinelibrary.wiley.com/doi/10.1002/aelm.202400095 by Kumoh National Institute, Wiley Online Library on [12/07/2024]. See the Terms and Conditions (https://onlinelibrary.wiley.com/terms-and-conditions) on Wiley Online Library for rules of use; OA articles are governed by the applicable Creative Commons License

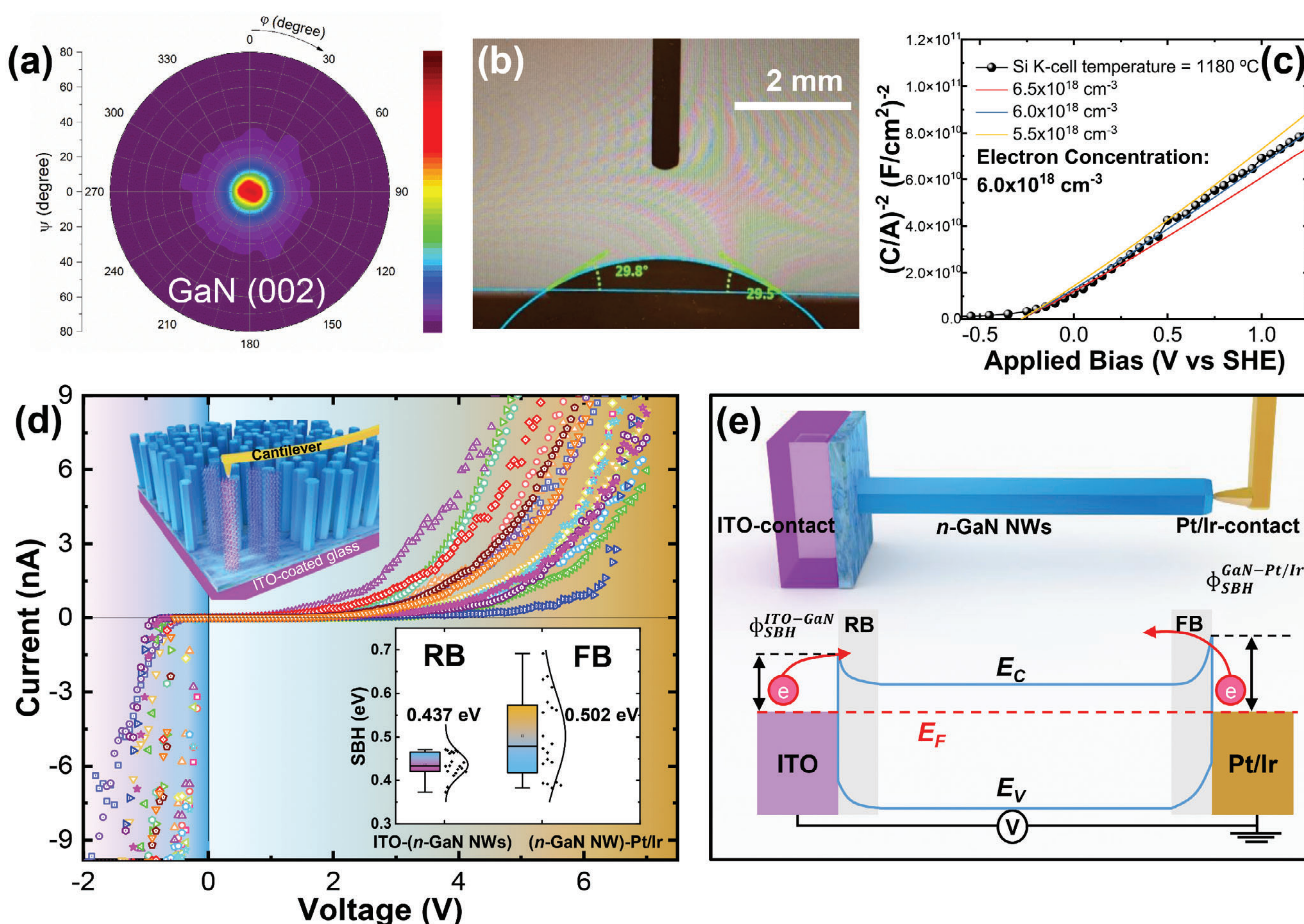

Figure 3. a) X-ray pole figure measurement for the (002) reflection. b) Measurement of water droplet contact angle. c) Mott–Schottky measurements at a Si K-cell temperature of 1180 °C with fitting curves for a fully elongated, 340 nm-thick GaN NWs-on-glass. d) Room-temperature *I*–*V* curves for 20 different *n*-GaN NWs. Insets show the ensemble schematic of GaN NWs-on-glass (top) and the average SBH values at both interfaces (bottom). e) Schematic illustration of *c*-AFM measurements on a single *n*-GaN NW (top) and a band diagram showing SBH formations at the (ITO-(*n*-GaN NWs)) and ((*n*-GaN NWs)-Pt/Ir) heterointerfaces, with no voltage or force applied (bottom).

for bare glass, ITO-coated glass, and various *n*-GaN structures. In Figure 2c, the bare glass and 200 nm-thick ITO-coated glass exhibit transmittance rates of 94.6% and 77.0%, respectively, for the visible light wavelength range.[19] For the comparison of transmittance, a GaN NWs-on-glass and a planar *n*-GaN layer on ITO-coated glass (GaN-on-glass) were prepared. Compared with other GaN-on-glass structures ($h = 50$ and 150 nm), the fully elongated ($h = 340$ nm) GaN NWs-on-glass shows enhanced transmittance due to the rough surface creating a graded refractive index at the air/NWs interface. However, high-density and inclined NWs tend to dissipate more light within the NWs, reducing transmittance below that of bare ITO-coated glass.[20] In Figure 2d, two GaN-on-glass samples exhibit weak band edge emission (BE) peaks at 3.4 eV and strong yellow luminescence (YL) peaks ≈2.34 eV, suggesting deficient crystallinity.[21] The disparity between the crystal structure of GaN and ITO might cause a high density of edge/screw dislocations within the crystal structure.[22] Conversely, NW structures show improved intensity of BE peaks, with BE intensity surpassing YL intensity in 150 nm-thick *n*-GaN NWs. Additionally, 340 nm-thick *n*-GaN NWs exhibit strong and narrow BE peaks and YL peaks, indicating significantly improved crystalline quality after NW elongation. Figure 2e summarizes the BE/YL ratio for various thicknesses of GaN-on-glass and GaN NWs-on-glass, suggesting that *n*-GaN NWs with a thickness of 340 nm achieve high crystalline quality as an epitaxial layer structure.

Additional structural, surface, and electrical characterizations were performed to evaluate the capabilities of the GaN NWs-on-glass as a transparent conductive platform. Despite the slanted formations of the NWs, X-ray pole figure analysis of the (002) reflection indicated a strong preference for the *c*-plane (002) orientation, in the axially grown *n*-GaN NWs, with most NWs growing perpendicular to the ITO surface, as shown in **Figure 3a**. The wettability of the *n*-GaN NWs ensemble was assessed using the sessile-drop contact angle measurement method, revealing a contact angle of 29.8° for a 5-µL water droplet, indicative of hydrophilic surface properties suitable for spin-coating perovskite materials (Figure 3b). Electron concentration within the ensemble was quantified by Mott–Schottky measurement,[23] with results shown in Figure 3c indicating heavy doping of the GaN

© 2024 The Authors. Advanced Electronic Materials published by Wiley-VCH GmbH

2199160x, 0, Downloaded from https://onlinelibrary.wiley.com/doi/10.1002/aelm.202400095 by Kumoh National Institute, Wiley Online Library on [12/07/2024]. See the Terms and Conditions (https://onlinelibrary.wiley.com/terms-and-conditions) on Wiley Online Library for rules of use; OA articles are governed by the applicable Creative Commons License

NWs-on-glass heated to a Si cell temperature of 1180 °C, resulting in an electron concentration of 6.0×10^{18} cm^{-3}. This supports the classification of the NWs as heavily doped *n*-type semiconductors (Section S3, Supporting Information). Conductive atomic force microscopy (*c*-AFM) was then used to study the contact behavior between *n*-GaN NWs and ITO. The Ohmic contact at the heterointerface between *n*-GaN/metal is notably challenging, often presenting a high Schottky barrier height (SBH) of ≈1 eV. Random sampling of 20 *n*-GaN NWs yielded current-voltage (*I*–*V*) curves that estimated the SBH formation at both interfaces of the *n*-GaN NWs ends (Figure 3d).[2d] According to the fitting results (Section S4, Supporting Information), the average SBH values at the ITO-(*n*-GaN NWs) and (*n*-GaN NW)-Pt/Ir heterointerfaces were 0.437 and 0.502 eV, respectively. The average SBH of 0.437 eV at the ITO-(*n*-GaN NWs) interface showed a similar value to other reported values for sputtered ITO on *n*-GaN (0.462 eV).[24] However, the observed average value of 0.502 eV at the (*n*-GaN NW)-Pt/Ir interface was lower than the theoretical prediction of $\Phi_{SBH}^{GaN-Pt/Ir}$(1 eV), with values ranging from 0.388 to 0.691 eV. This variation is attributed to the nano-sized Pt/Ir tip diameter (25 nm), which is smaller than the average diameter of the *n*-GaN NW (75 nm), leading to an unstable Schottky metal contact area during *c*-AFM measurement.[25] In conclusion, Mott-Schottky and *c*-AFM measurements confirmed that the *n*-GaN NWs are heavily doped, with an electron concentration of 6.0×10^{18} cm^{-3}, which facilitates thermionic-field emission as the dominant mechanism for electrical transport through the Schottky barriers at both ends of the *n*-GaN NWs.[26] Consequently, a perovskite/*n*-GaN heterostructure can be effectively formed by spin-coating on the hydrophilic GaN NWs-on-glass, allowing efficient electron transport from perovskite to the ITO interlayer through *n*-GaN, as the sufficiently narrow SB permits tunneling.[2d,26,27] Figure 3e illustrates a schematic representation of a single *n*-GaN NW on the ITO interlayer probed with a Pt/Ir-coated *c*-AFM tip (top), and suggests a schematic band diagram at a sample bias of 0 V and 0 nN applied force (bottom).[2d,27a,b]

2.3. Structural and Optical Characteristics of *n*-GaN/$MAPbI_3$ Heterostructure

In **Figure** 4a, bright-field scanning transmission electron microscopy (STEM) examined the cross-sectional view of an *n*-GaN NWs/$MAPbI_3$ heterostructure to observe each interface and confirm the infiltration of $MAPbI_3$ perovskite material into *n*-GaN NWs. Initially, it was confirmed that the *n*-GaN wetting layer is integrated between the ITO interlayer and the *n*-GaN NWs. Subsequent energy-dispersive X-ray spectroscopy (EDX) STEM images demonstrated that the *n*-GaN NWs remained intact after the $MAPbI_3$ spin-coating process, with each $MAPbI_3$ and ITO interlayer separated by *n*-GaN (Figure 4b,c). Moreover, the $MAPbI_3$ perovskite materials infiltrated well between the high-density, inclined *n*-GaN NWs. A magnified bright-field STEM image (Figure 4d) confirms that the *n*-GaN NWs are encapsulated by $MAPbI_3$ materials. White arrows within the *n*-GaN NWs indicate the well-known defects of basal-plane stacking faults (bSFs). These bSFs, indicative of mixed lattice stacking in wurtzite GaN crystals, are predominantly generated by the coalescence of inclined *n*-GaN NWs.[28] To further confirm the lattice structures, materials from *n*-GaN NWs (red rectangle) and $MAPbI_3$ perovskite (blue rectangle) were analyzed. From the high-resolution scanning transmission electron microscopy (HR-STEM) image, a *c*-plane oriented GaN lattice structure was confirmed, and an inset of the fast-Fourier transform (FFT) shows a wurtzite lattice structure (Figure 4e).[29] In Figure 4f, white solid lines mark the lattice interplanar spacing of ≈0.32 and 0.44 nm, with an inset of FFT confirming the *β*-phase tetragonal structure of $MAPbI_3$.[30] The optical properties of the *n*-GaN/$MAPbI_3$ heterostructure were assessed by comparing a $MAPbI_3$ light-absorber layer spin-coated on GaN-on-glass with that on the GaN NWs-on-glass, and a reference sample spin-coated on bare glass. Powder X-ray diffraction (XRD) patterns measured the crystal quality of $MAPbI_3$ and the GaN NWs-on-glass after spin-coating, confirming that each layer was well preserved without any signs of corrosion. In Figure 4g, the $MAPbI_3$ diffraction peaks align well with those of the tetragonal phase.[31] Comparative studies using PL intensity comparison and time-resolved PL (TR-PL) measurements of recombination dynamics (Figure 4h,i) showed that the GaN NWs-on-glass exhibited the lowest PL intensity and a shorter average decay time of 15.955 ns (Section S5 and Table S2, Supporting Information).[32] This suggests that the GaN NWs-on-glass more efficiently extracts photogenerated electrons from the perovskite medium. We speculate that these results are due to the different geometries of the planar layer and NWs platform. The high aspect ratio of NWs offers a larger contact area for the $MAPbI_3$ light-absorber layer at the $MAPbI_3$/*n*-GaN NWs interfaces. Consequently, the GaN NWs-on-glass platform was confirmed to be a better ETL with respect to carrier extraction efficiency when stacked with perovskite materials than the GaN-on-glass platform.

2.4. Fabrication and Optical Simulation of Perovskite-GaN Prototype Device

After confirming the infiltration behavior of $MAPbI_3$ into *n*-GaN NWs, a prototype device structure was proposed for demonstrating perovskite solar cells and photodetectors. **Figure** 5a illustrates a prototype device comprising an ITO interlayer on glass (transparent conducting layer, TCL), *n*-GaN NWs with a wetting layer (ETL), $MAPbI_3$ (light-absorbing layer), and Spiro-OMeTAD (HTL). Prior to device fabrication, a 3D-FDTD simulation was conducted on the $MAPbI_3$/GaN NWs heterostructures to study optical phenomena, using parameters for GaN and $MAPbI_3$ sourced from the literature.[33] A model structure, featuring a single GaN NW on a GaN wetting layer as an ETL is also depicted in Figure 5a and analyzed under UV and visible light illumination. In the FDTD simulation, light travels from the bottom of the glass, through the ITO interlayer (h = 200 nm) and GaN NWs, reaching the $MAPbI_3$ layer. The UV light (λ = 350 nm) degrades $MAPbI_3$ material quality; thus, the underlying layer absorbs almost all the UV light to protect the perovskite from degradation (Section S6 and Figure S5, Supporting Information).[34] Conversely, it allows visible light to pass through without absorption. The device's GaN wetting layer, with a bandgap energy of 3.4 eV, functions as both an ETL and an effective UV blocker, absorbing light below 380 nm. The simulations tested light propagation and absorption at the $MAPbI_3$/GaN heterostructure in

© 2024 The Authors. Advanced Electronic Materials published by Wiley-VCH GmbH

2199160x, 0, Downloaded from https://onlinelibrary.wiley.com/doi/10.1002/aelm.202400095 by Kumoh National Institute, Wiley Online Library on [12/07/2024]. See the Terms and Conditions (https://onlinelibrary.wiley.com/terms-and-conditions) on Wiley Online Library for rules of use; OA articles are governed by the applicable Creative Commons License

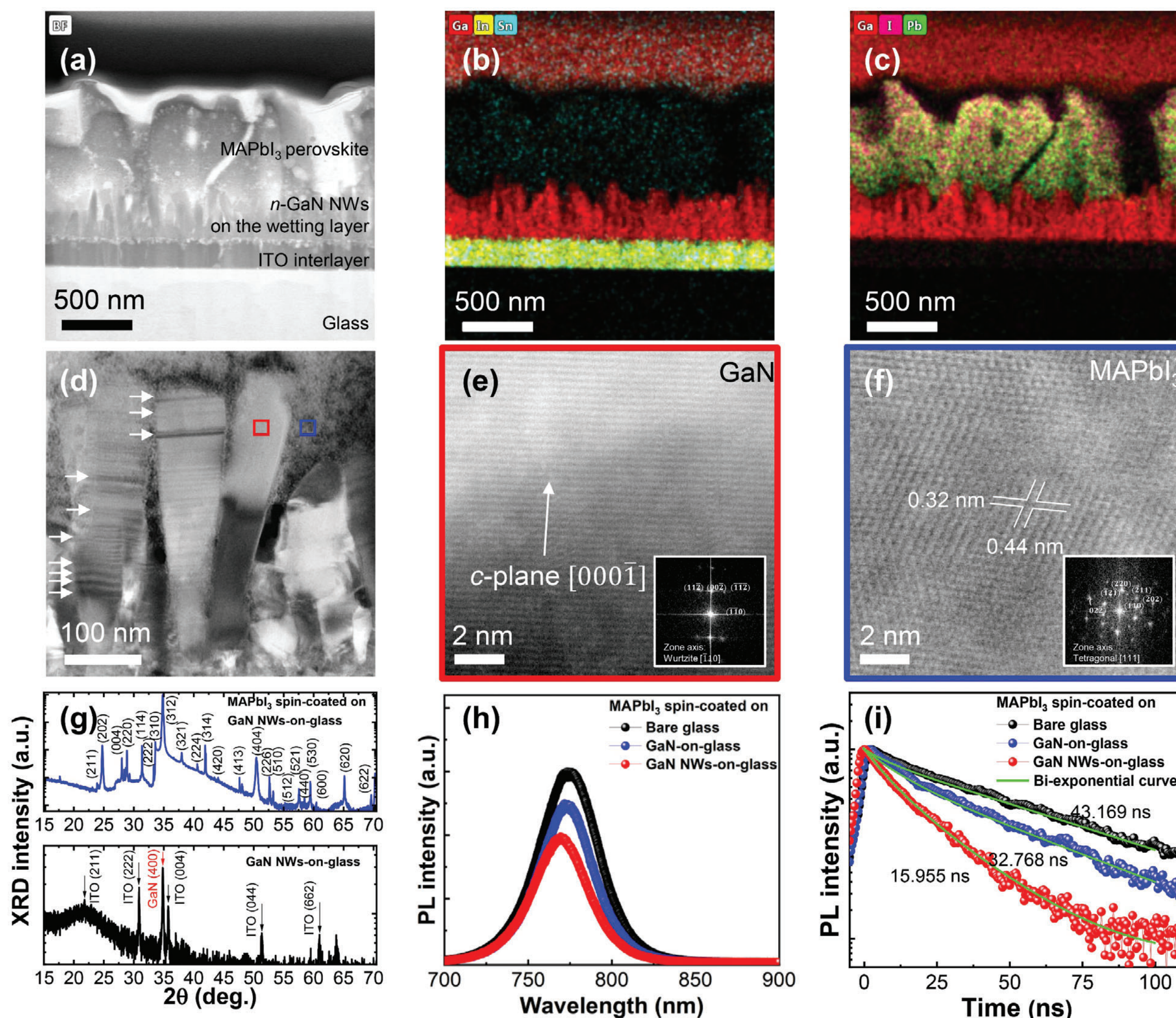

Figure 4. a) Bright-field STEM image of a prototype device following the spin-coating of $MAPbI_3$ material, with accompanying STEM-EDX elemental mapping of b) Ga, In, Sn, and c) Ga, I, and Pb atoms. d) A detailed bright-field STEM image reveals the *n*-GaN NWs and $MAPbI_3$ materials. White arrows highlight bSF defects within the *n*-GaN NWs. e) HR-STEM image illustrating the lattice structure within *n*-GaN NWs (highlighted by a red rectangle in Figure 4d), including an inset showing the FFT analysis of the wurtzite crystal structure of GaN. f) HR-STEM image displaying the lattice of $MAPbI_3$ (marked by a blue rectangle in Figure 4d), with an inset showing the FFT of the tetragonal phase of the $MAPbI_3$ lattice. g) Powder XRD patterns of the *n*-GaN NWs and $MAPbI_3$ spin-coated on the GaN NWs-on-glass. h) Steady-state PL spectrum, and i) Normalized TR-PL decay curve for $MAPbI_3$ on various substrates: bare glass, GaN-on-glass, and GaN NWs-on-glass.

three GaN nanostructures: GaN-on-glass (h = 300 nm, left), GaN NWs-on-glass (h = 270 nm for NWs and 70 nm for the wetting layer, center), and pristine GaN NWs (h = 270 nm, right), each at different thicknesses and exposed to various wavelengths (λ = 350, 400, 530, and 660 nm), respectively (Figure 5b,c). The wetting layer thickness was set at 70 nm due to coalescence at the early stage of NWs growth (Figure S3, Supporting Information). The $MAPbI_3$ layer's height (400 nm) on GaN NWs was considered thinner since the $MAPbI_3$ materials infiltrated between NWs. For all GaN configurations, the electric (***E***)-field profile of $MAPbI_3$ perovskite is intensified at the interface with GaN due to the high refractive index of GaN, enhancing light refraction (Figure 5b). As the incident light wavelength increases, the enhanced ***E***-field position shifts deeper into the GaN NW structures.

The light absorption profiles in Figure 5c indicate that both the GaN-on-glass and GaN NWs-on-glass effectively absorb UV light at 350 nm, almost preventing it from reaching the $MAPbI_3$ layer. However, the pristine GaN NWs do not block UV light due to the absence of a GaN wetting layer. The simulation also showed that the visible light wavelengths above 400 nm are predominantly absorbed by the $MAPbI_3$ layer. Notably, the light absorption by $MAPbI_3$ is enhanced along the *m*-plane facet of the GaN NW on the wetting layer, whereas the pristine GaN NWs show weaker absorption at the bottom. The study summarized the optical phenomena of light propagation and absorption in the $MAPbI_3$/GaN NW heterostructures using GaN NW ETLs with and without a wetting layer, compared to a planar GaN layer. The 70 nm-thick wetting layer effectively blocks UV light, enhancing light

 © 2024 The Authors. Advanced Electronic Materials published by Wiley-VCH GmbH

ADVANCED ELECTRONIC MATERIALS Open Access
www.advelectronicmat.de

2199160x, 0, Downloaded from https://onlinelibrary.wiley.com/doi/10.1002/aelm.202400095 by Kumoh National Institute, Wiley Online Library on [12/07/2024]. See the Terms and Conditions (https://onlinelibrary.wiley.com/terms-and-conditions) on Wiley Online Library for rules of use; OA articles are governed by the applicable Creative Commons License

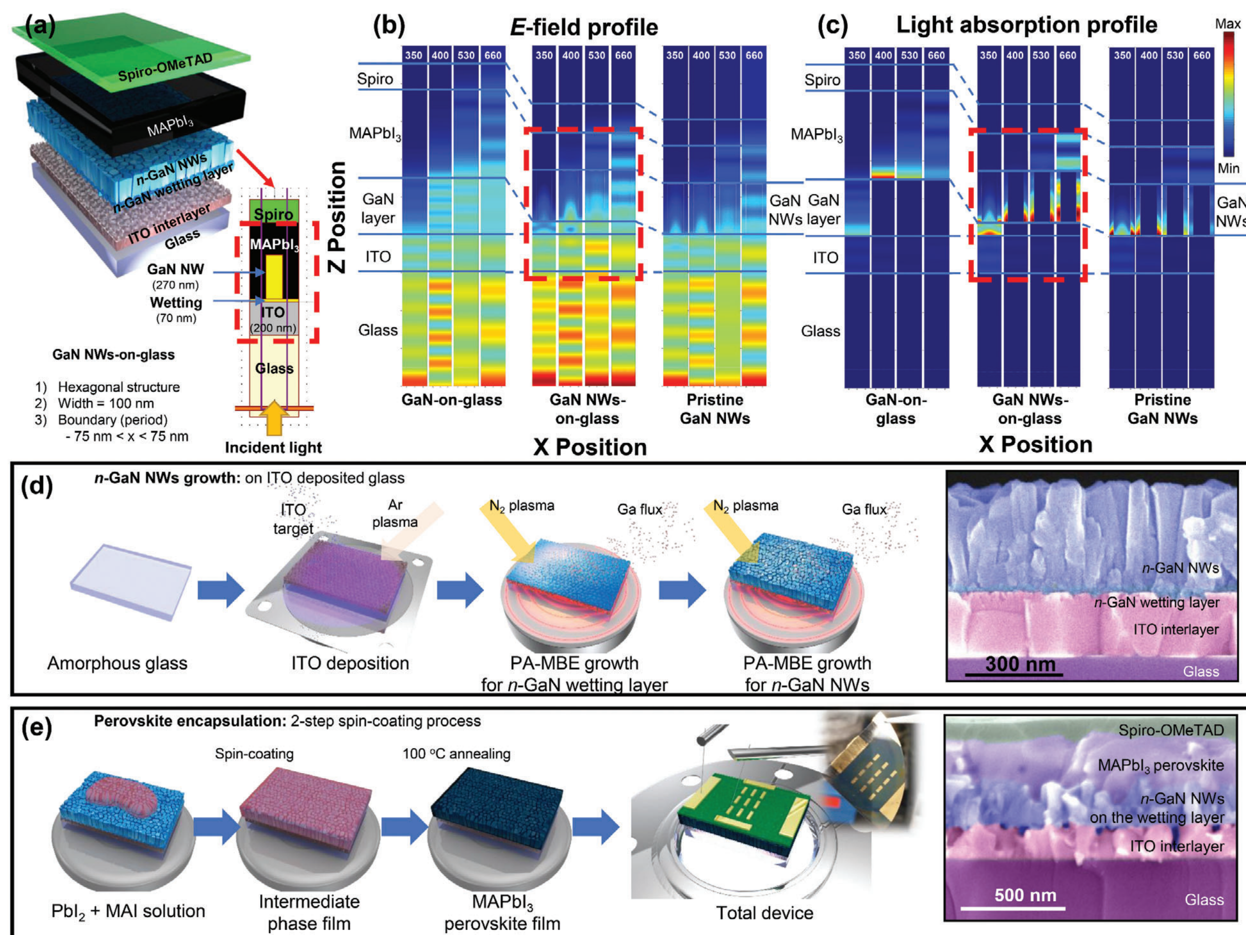

Figure 5. Schematics of a) a prototype device alongside an optical simulation model for 3D-FDTD. Three distinct GaN structures are illustrated: a GaN-on-glass (left), GaN NWs-on-glass (center), and pristine GaN NWs (right) for b) an *E*-field profile and c) a light absorption profile. These structures were simulated at monochromatic wavelengths of 350, 400, 530, and 660 nm. The red dashed rectangle identifies the GaN NWs (270 nm) ETL on a wetting layer (70 nm). The schematic also outlines d) the deposition of the ITO layer on glass via RF magnetron sputtering and the growth of *n*-GaN NWs on ITO-coated glass by PA-MBE. e) Details the $MAPbI_3$ perovskite spin-coating process and its measurement overview. Insets display false-color cross-sectional SEM images of the GaN NWs-on-glass and an overview of a prototype device.

absorption along the vertical facet of the NW. The entire fabrication process is detailed in Figure 5d,e. A pseudo-color SEM cross-sectional view (inset of Figure 5d) shows a collection of epitaxially grown *n*-GaN NWs, with a density of 1.60×10^9 cm^{-2} and a filling factor of 45.5%. A quarter of a 2-inch GaN NWs-on-glass was cleaned using solvents and exposed to oxygen plasma to enhance hydrophilicity. The prototype device structure was then fabricated using an anti-solvent approach for $MAPbI_3$ deposition, followed by the Spiro-OMeTAD spin-coating process. The process flow, illustrated in Figure 5e, and a cross-sectional SEM view highlight each layer's role in the device structure.

2.5. $MAPbI_3$ Perovskite Device Applications Based on the *n*-GaN NWs ETL

To evaluate our studies on $MAPbI_3$/*n*-GaN NW heterostructures, prototype device structures were assessed using current density-voltage (*J*–*V*) and external quantum efficiency (EQE) measurements. We constructed devices for perovskite solar cells in three distinct configurations of *n*-GaN ETL nanostructures: solely *n*-GaN NWs (pristine GaN NWs), GaN-on-glass, and GaN NWs-on-glass. **Figure 6a** illustrates the *J-V* characteristics of $MAPbI_3$ perovskite solar cells with various *n*-GaN ETL nanostructure types and lengths. Notably, PSCs with pristine GaN NWs lacking a wetting layer (the green curve) displayed the lowest fill factor (FF) and power conversion efficiency (PCE). As previously mentioned, spin-coated $MAPbI_3$ perovskite infiltrates well between *n*-GaN NWs, allowing direct contact with the ITO interlayer due to the absence of an *n*-GaN wetting layer. Consequently, pristine GaN NWs do not prevent the flow of holes from $MAPbI_3$ to ITO.[35] Subsequently, we explored the effects of GaN-on-glass and thicknesses of GaN NWs-on-glass ETLs. In this context, PSCs featuring a 340 nm-thick GaN NWs-on-glass ETL exhibited superior performance with a reverse-scan short-circuit current density (J_{sc}) of 19.60 mA·cm^{-2}, open-circuit voltage (V_{oc}) of 1.078 V, and *FF* of 74.2%. These figures significantly exceeded those of PSCs using a 1255 nm-thick GaN NWs-on-glass ETL, likely due

 © 2024 The Authors. Advanced Electronic Materials published by Wiley-VCH GmbH

ADVANCED ELECTRONIC MATERIALS
Open Access
www.advelectronicmat.de

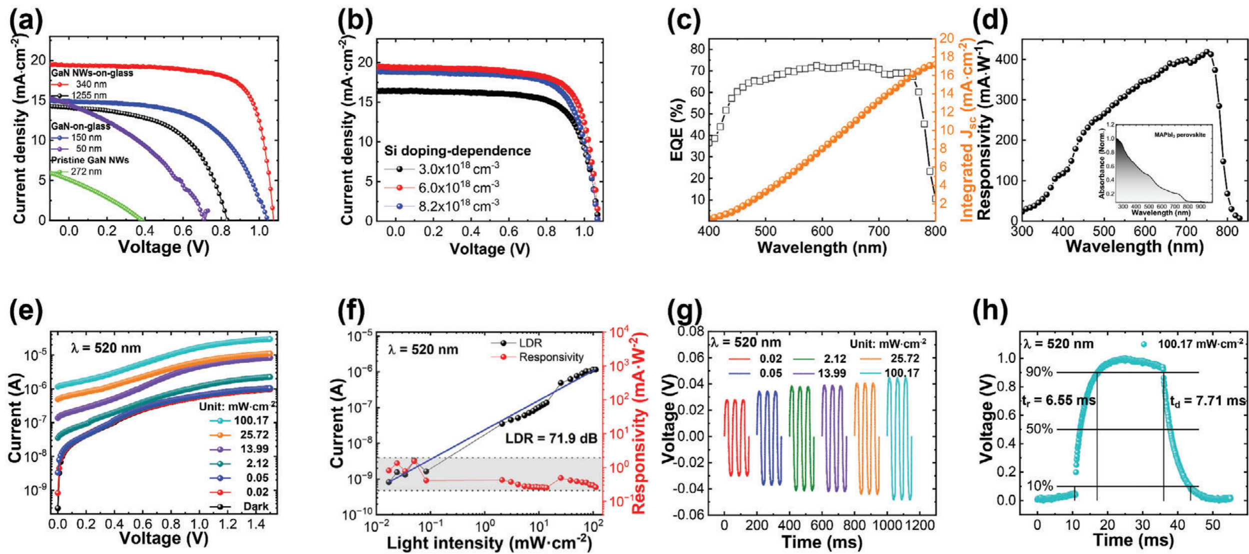

Figure 6. a) *J–V* characteristics of $MAPbI_3$ PSCs with *n*-GaN nanostructure ETLs, featuring heights of 340 and 1255 nm for GaN NWs-on-glass, 50 and 150 nm for GaN-on-glass, and 272 nm for pristine GaN NWs. b) Three different Si doping concentrations of GaN NWs-on-glass ETL and corresponding photovoltaic parameters under AM1.5G with 1 sun illumination. c) EQE spectra and the integrated J_{sc} of the champion cell. d) Spectral responsivity and absorption spectra (inset shown). e) *I–V* curves under various light intensities and f) linear dynamic range and responsivity measurements conducted with a 520 nm laser. g) Temporal response investigated under various light intensities of a 520 nm laser with 20 Hz modulation and h) rise and fall times calculated at a light intensity of 100.17 mW·cm^{-2} (20 Hz). All measurements were performed without applying any bias.

to the diffusion length limitation of photo-excited carriers below 450 nm in *n*-GaN at room temperature (Table S3, Supporting Information).[36] Our findings underscore a critical length dependency of *n*-GaN NWs when paired with a perovskite active layer. As previously confirmed by 3D-FDTD simulations, the PSC with a 340 nm-thick GaN NWs-on-glass ETL also exhibited performance compared to PSCs with a GaN-on-glass ETL. Additionally, we investigated PCE for different electron concentrations in GaN NWs-on-glass, as depicted in Figure 6b. Optimizing the doping strategy improved the ionized carrier concentration, enhancing injection efficiency and emphasizing the importance of precise doping quantification for device applications. Using Mott-Schottky analysis,[23] we measured the electron concentration in GaN NWs-on-glass. $MAPbI_3$ PSCs with an electron concentration of 6.0×10^{18} cm^{-3} demonstrated notable improvements in J_{sc}, V_{oc}, and *FF* (Table S3, Supporting Information). The PCE of these solar cells increased from 12.52% to 15.67% before declining to 14.41% as the electron concentration rose. Excessive Si doping in GaN NWs often leads to severe coalescence with adjacent NWs (Figure S4, Supporting Information),[37] resulting in optical loss and reduced transmittance that impair carrier extraction efficiency. The corresponding EQE and integrated J_{sc} of the best-performing PSC are presented in Figure 6c. This top PSC, featuring a GaN NWs-on-glass ETL, demonstrated an electron concentration of 6.0×10^{18} cm^{-3} and a height of ≈340 nm. In the visible wavelength range without bias, the EQE surpassed 65%, peaking at 71.9% at 680 nm, suggesting the device's potential as a photodetector. The responsivity value, calculated from the measured EQE,[38] can be derived using the specified equation.

$$R = \frac{J_{light}}{P_{beam}} = \frac{EQE \times \lambda e}{hc \times 100} \tag{2}$$

where J_{light} is the photocurrent density, P_{beam} is the illuminated power density under a specific wavelength of incident light, e is the electron charge, h is the Planck constant, and c is the speed of light. Figure 6d shows the spectral responsivity of a prototype device at 0 V, which linearly increased from 300 to 800 nm, peaking at 420 mA·W^{-1} at 750 nm. This trend aligns well with previous studies using $MAPbI_3$ as an active medium for photodetection.[10,39] The inset displays the absorption spectra of $MAPbI_3$/*n*-GaN NWs, indicating strong absorption within the 300–800 nm range. To further examine the photoresponse, *I–V* curves were measured in the dark and under varying light intensities using a 520 nm laser at 0 V (Figure 6e), showing increased photocurrent with light intensity due to more photogenerated carriers. The linear dynamic range (LDR), a key performance metric for photodetectors, maintained constant responsivity over a broad light intensity spectrum. The LDR is described as:

$$LDR = 20 \log \left(\frac{P_{sat}}{P_{low}} \right) \tag{3}$$

where P_{sat} and P_{low} denote the light intensities where the current starts to deviate from the linear region and the lowest measured light intensity, respectively.[40] In Figure 6f, the LDR was recorded under a 520 nm laser with light intensities ranging from 0.02 to 111.8 mW·cm^{-2}, achieving a value of 71.9 dB. Responsivity is also measured as a function of light intensity, showing a difference of 1.3 mA·W^{-1} (grey area). The slight difference could be attributed to the stability of the perovskite material and measurement error.[41] For the temporal response, the laser mode was switched to pulse mode with modulation at 20 Hz. A sine waveform was applied to the device, with intensity increasing alongside the light intensity (Figure 6g). The rise and fall times

© 2024 The Authors. Advanced Electronic Materials published by Wiley-VCH GmbH

2199160x, 0, Downloaded from https://onlinelibrary.wiley.com/doi/10.1002/aelm.202400095 by Kumoh National Institute, Wiley Online Library on [12/07/2024]. See the Terms and Conditions (https://onlinelibrary.wiley.com/terms-and-conditions) on Wiley Online Library for rules of use; OA articles are governed by the applicable Creative Commons License

(denoted as t_r and t_d) were determined to be 6.55 and 7.71 ms, respectively, based on the curve fitting in Figure 6h.

3. Conclusion

In summary, *n*-GaN nanowires were grown on ITO-coated glass using PA-MBE, with $MAPbI_3$ subsequently spin-coated onto GaN NWs-on-glass to investigate the band alignment of the *n*-GaN/$MAPbI_3$ heterostructure. It was found that $MAPbI_3$ perovskites infiltrated well between the *n*-GaN nanowires, with the structural properties analyzed using cross-sectional HRTEM. XPS measurements indicated a VBO of 2.19 eV and a CBO of 0.40 eV, suggesting a type-II band alignment. Prior to device fabrication, carrier extraction and photon recycling enhancements were confirmed through PL measurements and FDTD simulations. A prototype device was fabricated, making the first demonstration of heterogeneous integration of bottom-up *n*-GaN NWs with $MAPbI_3$. This approach merges these promising materials, aiming to overcome the limitations of both GaN (low PCE in GaN-based solar cells, <3%) and perovskite (lack of durable ETL) materials on ITO-coated glass. This study presents a novel method for integrating GaN-based wide bandgap materials with other systems, enhancing their practical applications.

4. Experimental Section

$MAPbI_3$/GaN Heterostructure Band Alignment Measurement by XPS: XPS was carried out using a Kratos Axis Supra DLD spectrometer with a monochromatic Al Kα X-ray source ($h\nu$ = 1486.6 eV) at 45 W, a multichannel plate, and a delay line detector in a vacuum of $\approx 10^{-9}$ mBar. Electrochemical impedance spectroscopy (EIS; Nyquist and Mott-Schottky measurements) was used to estimate the ionized carrier concentration of *n*-GaN NWs in dark conditions. The SBH was determined through *c*-AFM (using an Agilent 5500 SPM) equipped with an Sb-doped Si probe and a conductive Pt/Ir tip (CONTV-PT).

Growth of n-GaN NWs and Wetting Layer: Si-doped *n*-type GaN NWs were grown on ITO-coated 2-inch glass (fused silica) using a Veeco GEN 930 PA-MBE system. The NWs were grown at 700 °C for 2 h, following a 10 min growth of a *n*-GaN wetting layer at 500 °C. This layer was placed between the *n*-GaN NWs and the ITO interlayer. The deposition and growth procedures for the *n*-GaN NWs and the wetting layer are detailed schematically (Figure 5d), with full procedures available elsewhere.[2b] For comparison, while the *n*-GaN wetting layer's growth time was consistently 10 min, the *n*-GaN NWs' growth time was varied to adjust the NWs' length. The temperature of the Si dopant cell ranged from 1165 to 1210 °C, varying the electron concentration in GaN.

c-AFM Measurement for n-GaN NWs: A 1 × 1 cm^2 sample of the GaN NWs-on-glass was prepared for *c*-AFM measurements. The sample was treated with a 10% KOH solution to remove the surface oxide and reduce contact resistance. Subsequently, 5 nm of Ni and 5 nm of Au were deposited using the oblique angle deposition technique of an e-beam evaporator. *c*-AFM measurements were performed using an Agilent 5500c SPM, and Pt–Ir coated, antimony-doped silicon probes were used (Bruker CONTV-PT). Detailed procedures are available elsewhere.[42]

Device Fabrication with $MAPbI_3$ Perovskite: The spin-coating process and device fabrication steps are illustrated in Figure 5e. Methylammonium iodide (MAI) was sourced from Greatcell Solar Limited, Australia, and lead (II) iodide (PbI_2, 99.999%, ultradry) was obtained from Alfa Aesar. γ-Butyrolactone (GBL, >99%) was procured from Sigma–Aldrich. All materials were used as received without additional purification. Before spin-coating $MAPbI_3$, the GaN NWs-on-glass were cleaned using O_2 plasma treatment for 5 min. $MAPbI_3$ films were created using an antisolvent extraction approach in an N_2 glove box. The $MAPbI_3$ perovskite precursor solution was made by dissolving 461 mg of PbI_2 and 159 mg of MAI in 700 µL of dimethylformamide (DMF) and 78 µL of dimethyl sulfoxide (DMSO). The solution (100 µL) was spin-coated onto the *n*-GaN nanowires at 4000 rpm for 20 s, followed by a quick chlorobenzene wash (200 µL) after 6 s of spinning. The sample was then annealed at 100 °C for 15 min. Spiro-OMeTAD (50 nm) was prepared as previously reported[43] and applied over the $MAPbI_3$ layer at 4000 rpm for 60 s. Finally, Au (80 nm) was deposited via thermal evaporation at a high vacuum of 3.0×10^{-6} Torr.

Materials Characterization: The sample's transmittance and absorption were measured using a UV–vis–NIR spectrophotometer (UV-3600, SHIMADZU, Japan). The morphology of the *n*-GaN NWs and the subsequent prototype devices was characterized using SEM (Zeiss Merlin, Jena, Germany). HR-STEM and elemental mapping were performed via STEM-EDX spectroscopy using a TEM (Titan Themis Z, Thermo Fisher Scientific, USA). Temperature-dependent PL measurements were conducted in a helium-cooled closed-loop refrigerator (Janis Cryostat: CCS-XG-M/204N) using a third harmonic signal (λ = 260 nm) from a mode-locked Ti:Sapphire laser (Coherent Mira-HP) with an output power of 3.5 W (λ = 780 nm). Emissions were detected by QEPro (Ocean Optics). TR-PL utilized a second harmonic generator (APE-SHG/THG, λ = 400 nm) from a mode-locked Ti:Sapphire laser (Coherent Mira 900) with an output power of 1.9 W (λ = 800 nm), with emissions detected by a streak camera (Hamamatsu C6860). The crystallinity of the sample was verified using powder XRD (Bruker D8 ADVANCES) with CuK_α radiation. Temperature-dependent XRD measurements were performed with a Bruker D8 Advance 2 equipped with an HTK 1200N furnace. XRD pole figures were examined using a Bruker D8 Discover Ultra with Cu Kα radiation (λ = 1.5406 Å), collecting data across a full φ-scan in the χ range from 0 to 50° using a LYNXEYE_XE detector in 0D mode.

Optical Simulation: FDTD simulations (FullWave, RSoft Design Group, USA) were conducted to determine the light absorption profile across various thicknesses and shapes of the GaN/$MAPbI_3$ heterostructure on ITO-coated glass. The simulations were set up with domain sizes of 150 nm in the *x* and *y* directions, respectively, and a 1 nm grid size. Perfectly matched layer (PML) boundary conditions were used to isolate the computational regions. The incident light was directed from the bottom glass layer to the top $MAPbI_3$ perovskite layer, with both transverse electric (TE) and transverse magnetic (TM) polarization modes averaged to simulate unpolarized light. A wave propagation monitor on the *xz* plane (y = 0) was used to measure the spatial absorption profile.

Solar Cell and Photodetector Device Test: Photovoltaic characterization was conducted using a Class AAA solar simulator equipped with a 150 W Xenon lamp (Sun 3000, Abet Technologies) under AM1.5G illumination. *I–V* characteristics were measured with a Keithley 2500 source meter, and light intensity was calibrated using a silicon reference cell with a KG5 filter window (ReRa Solutions). The EQE was addressed using a spectral response measurement system (QEX10, PV Measurements, Inc.). For speed measurements, the photocurrent was recorded at various excitation power densities up to 111.8 mW·cm^{-2} with a fixed excitation wavelength of 520 nm from a single mode laser diode (Thorlabs, LP520-SF15). All measurements were conducted without applying a bias voltage.

Supporting Information

Supporting Information is available from the Wiley Online Library or from the author.

Acknowledgements

The authors would like to acknowledge support supported by the National Research Foundation of Korea (NRF) grant funded by the Korea government (MSIT) (RS-2023-00244550, 2009–0082580).

Conflict of Interest

The authors declare no conflict of interest.

 © 2024 The Authors. Advanced Electronic Materials published by Wiley-VCH GmbH

2199160x, 0, Downloaded from https://onlinelibrary.wiley.com/doi/10.1002/aelm.202400095 by Kumoh National Institute, Wiley Online Library on [12/07/2024]. See the Terms and Conditions (https://onlinelibrary.wiley.com/terms-and-conditions) on Wiley Online Library for rules of use; OA articles are governed by the applicable Creative Commons License

Data Availability Statement

The data that support the findings of this study are available from the corresponding author upon reasonable request.

Keywords

electron transport layer, GaN nanowires, GaN-on-glass, $MAPbI_3$, photodetector, solar cell

Received: February 12, 2024
Revised: May 3, 2024
Published online:

[1] S. Nakamura, T. Mukai, M. Senoh, *Appl. Phys. Lett.* **1994**, *64*, 1687.
[2] a) J. H. Choi, A. Zoulkarneev, S. I. Kim, C. W. Baik, M. H. Yang, S. S. Park, H. Suh, U. J. Kim, H. Bin Son, J. S. Lee, *Nat. Photon.* **2011**, *5*, 763; b) A. Prabaswara, J.-W. Min, R. C. Subedi, M. Tangi, J. A. Holguin-Lerma, C. Zhao, D. Priante, T. K. Ng, B. S. Ooi, *Nanoscale Res. Lett.* **2019**, *14*, 45; c) A. Prabaswara, J.-W. Min, C. Zhao, B. Janjua, D. Zhang, A. M. Albadri, A. Y. Alyamani, T. K. Ng, B. S. Ooi, *Nanoscale Res. Lett.* **2018**, *13*, 41; d) A. Prabaswara, H. Kim, J.-W. Min, R. C. Subedi, D. H. Anjum, B. Davaasuren, K. Moore, M. Conroy, S. Mitra, I. S. Roqan, *ACS Nano* **2020**, *14*, 2202; e) J. W. Shon, J. Ohta, K. Ueno, A. Kobayashi, H. Fujioka, *Sci. Rep.* **2014**, *4*, 5325.
[3] a) A. Y. Alsalloum, B. Turedi, X. Zheng, S. Mitra, A. A. Zhumekenov, K. J. Lee, P. Maity, I. Gereige, A. AlSaggaf, I. S. Roqan, *ACS Energy Lett.* **2020**, *5*, 657; b) K. J. Lee, J.-W. Min, B. Turedi, A. Y. Alsalloum, J.-H. Min, Y. J. Kim, Y. J. Yoo, S. Oh, N. Cho, R. C. Subedi, *ACS Energy Lett.* **2020**, *5*, 3295.
[4] J. Gong, S. Liu, Y. He, X. Feng, X. Xia, Z. Quan, L. Wang, *Appl. Phy. Lett.* **2017**, *111*, 122103.
[5] Q. Liu, Y. Q. Yang, X. Wang, W. Song, X. Luo, J. Guo, J. Shi, C. Cheng, D. Li, L. He, *J. Alloys and Comp.* **2021**, *864*, 158710.
[6] H. Wei, J. Wu, P. Qiu, S. Liu, Y. He, M. Peng, D. Li, Q. Meng, F. Zaera, X. Zheng, *J. Mater. Chem. A* **2019**, *7*, 25347.
[7] L. Zhao, Y. Gao, M. Su, Q. Shang, Z. Liu, Q. Li, Q. Wei, M. Li, L. Fu, Y. Zhong, *ACS Nano* **2019**, *13*, 10085.
[8] L. Su, Y. Zhang, J. Xie, *J. Mater. Chem. C* **2022**, *10*, 1349.
[9] S. Mitra, M. M. Muhammed, N. Alwadai, D. R. Almalawi, B. Xin, Y. Pak, I. S. Roqan, *RSC Adv.* **2020**, *10*, 6092.
[10] H. Zhou, J. Mei, M. Xue, Z. Song, H. Wang, *The J. Phys. Chem. C* **2017**, *121*, 21541.
[11] S. Chen, C. Zhang, J. Lee, J. Han, A. Nurmikko, *Adv. Mater.* **2017**, *29*, 1604781.
[12] E. Kraut, R. Grant, J. Waldrop, S. Kowalczyk, *Phys. Rev. Lett.* **1980**, *44*, 1620.
[13] O. Landré, R. Songmuang, J. Renard, E. Bellet-Amalric, H. Renevier, B. Daudin, *Appl. Phys. Lett.* **2008**, *93*, 183109.
[14] a) Y. Lu, X. Liu, D.-C. Lu, H. Yuan, Z. Chen, T. Fan, Y. Li, P. Han, X. Wang, D. Wang, *J. crystal growth* **2002**, *236*, 77; b) T. Stoica, E. Sutter, R. J. Meijers, R. K. Debnath, R. Calarco, H. Lüth, D. Grützmacher, *Small* **2008**, *4*, 751; c) F. Chen, S. Sun, X. Deng, K. Fu, G. Yu, L. Song, R. Hao, Y. Fan, Y. Cai, B. Zhang, *AIP Adv.* **2017**, *7*, 125018.
[15] H. Amano, N. Sawaki, I. Akasaki, Y. Toyoda, *Appl. Phys. Lett.* **1986**, *48*, 353.
[16] a) S. Hasegawa, S. Nishida, T. Yamashita, H. Asahi, *Thin Solid Films* **2005**, *487*, 260; b) T. Yamashita, S. Hasegawa, S. Nishida, M. Ishimaru, Y. Hirotsu, H. Asahi, *Appl. Phys. Lett.* **2005**, *86*, 082109; c) J. Bian, L. Miao, F. Qin, D. Zhang, W. Liu, H. Liu, *Mater. sci. semiconductor processing* **2014**, *26*, 182.
[17] J.-W. Min, D. Priante, M. Tangi, G. Liu, C. H. Kang, A. Prabaswara, C. Zhao, L. Al-Maghrabi, Y. Alaskar, A. M. Albadri, *J. Nanophoton.* **2018**, *12*, 1.
[18] a) M. Musolino, A. Tahraoui, S. Fernández-Garrido, O. Brandt, A. Trampert, L. Geelhaar, H. Riechert, *Nanotechnology* **2015**, *26*, 085605; b) R. Songmuang, O. Landré, B. Daudin, *Appl. Phys. Lett.* **2007**, *91*, 251902; c) H. Tambo, H. Asahi, *J. Crystal Growth* **2013**, *383*, 57.
[19] V. Teixeira, H. Cui, L. Meng, E. Fortunato, R. Martins, *Thin Solid Films* **2002**, *420*, 70.
[20] C. Chen, B. Hu, Z. Wang, X. Lv, C. Zhang, B. Chen, H. San, W. Hofmann, *Nano Energy* **2019**, *65*, 104042.
[21] A. L. Mulyo, Y. Konno, J. S. Nilsen, A. T. van Helvoort, B.-O. Fimland, H. Weman, K. Kishino, *J. Crystal Growth* **2017**, *480*, 67.
[22] O. Contreras, F. Ponce, J. Christen, A. Dadgar, A. Krost, *Appl. Phys. Lett.* **2002**, *81*, 4712.
[23] a) C. Zhao, M. Ebaid, H. Zhang, D. Priante, B. Janjua, D. Zhang, N. Wei, A. A. Alhamoud, M. K. Shakfa, T. K. Ng, *Nanoscale* **2018**, *10*, 15980; b) H. Zhang, M. Ebaid, J.-W. Min, T. K. Ng, B. S. Ooi, *J. Appl. Phys.* **2018**, *124*, 083105; c) H. Zhang, M. Ebaid, J. Tan, G. Liu, J.-W. Min, T. K. Ng, B. S. Ooi, *Opt. Express* **2019**, *27*, A81.
[24] Y.-Z. Chiou, J.-J. Tang, *Japanese J. Appl. Phys.* **2004**, *43*, 4146.
[25] N. Jamond, P. Chrétien, L. Gatilova, E. Galopin, L. Travers, J.-C. Harmand, F. Glas, F. Houzé, N. Gogneau, *Nanoscale* **2017**, *9*, 4610.
[26] G. Greco, F. Iucolano, F. Roccaforte, *Appl. Surf. Sci.* **2016**, *383*, 324.
[27] a) L. Al-Maghrabi, C. Huang, D. Priante, M. Tian, J.-W. Min, C. Zhao, H. Zhang, R. C. Subedi, H. H. Alhashim, H. Sun, *AIP Adv.* **2020**, *10*, 055014; b) M. Tangi, J.-W. Min, D. Priante, R. C. Subedi, D. H. Anjum, A. Prabaswara, N. Alfaraj, J. W. Liang, M. K. Shakfa, T. K. Ng, *Nano Energy* **2018**, *54*, 264; c) M. Heilmann, A. M. Munshi, G. Sarau, M. Göbelt, C. Tessarek, V. T. Fauske, A. T. van Helvoort, J. Yang, M. Latzel, B. r. Hoffmann, *Nano Lett.* **2016**, *16*, 3524.
[28] a) V. Consonni, M. Knelangen, U. Jahn, A. Trampert, L. Geelhaar, H. Riechert, *Appl. Phys. Lett.* **2009**, *95*, 241910; b) R. Liu, A. Bell, F. Ponce, C. Chen, J. Yang, M. A. Khan, *Appl. Phys. Lett.* **2005**, *86*, 021908; c) F. Meng, M. Estruga, A. Forticaux, S. A. Morin, Q. Wu, Z. Hu, S. Jin, *ACS Nano* **2013**, *7*, 11369.
[29] a) K. Goodman, V. Protasenko, J. Verma, T. Kosel, G. Xing, D. Jena, *J. Cryst. Growth* **2011**, *334*, 113; b) K. Lekhal, S.-Y. Bae, H.-J. Lee, T. Mitsunari, A. Tamura, M. Deki, Y. Honda, H. Amano, *J. Cryst. Growth* **2016**, *447*, 55.
[30] a) Y. Zhou, M. Yang, W. Wu, A. L. Vasiliev, K. Zhu, N. P. Padture, *J. Mater. Chem. A* **2015**, *3*, 8178; b) Z. Fan, H. Xiao, Y. Wang, Z. Zhao, Z. Lin, H.-C. Cheng, S.-J. Lee, G. Wang, Z. Feng, W. A. Goddard III, *Joule* **2017**, *1*, 548.
[31] a) J. Yu, X. Chen, Y. Wang, H. Zhou, M. Xue, Y. Xu, Z. Li, C. Ye, J. Zhang, P. A. Van Aken, *J. Mater. Chem. C* **2016**, *4*, 7302; b) R. K. Upadhyay, A. P. Singh, D. Upadhyay, S. Ratan, C. Kumar, S. Jit, *IEEE Photonics Technol. Lett.* **2019**, *31*, 1151.
[32] a) X. Li, J. Yang, Q. Jiang, H. Lai, S. Li, J. Xin, W. Chu, J. Hou, *ACS Nano* **2018**, *12*, 11022; b) L. Yan, Q. Xue, M. Liu, Z. Zhu, J. Tian, Z. Li, Z. Chen, Z. Chen, H. Yan, H. L. Yip, *Adv. Mater.* **2018**, *30*, 1802509.
[33] a) Y. J. Kim, G. J. Lee, S. Kim, J.-W. Min, S. Y. Jeong, Y. J. Yoo, S. Lee, Y. M. Song, *ACS Appl. Mater. Interfaces* **2018**, *10*, 28672; b) A. M. Leguy, P. Azarhoosh, M. I. Alonso, M. Campoy-Quiles, O. J. Weber, J. Yao, D. Bryant, M. T. Weller, J. Nelson, A. Walsh, *Nanoscale* **2016**, *8*, 6317.
[34] a) Y. Li, X. Xu, C. Wang, B. Ecker, J. Yang, J. Huang, Y. Gao, *J. Phys. Chem. C* **2017**, *121*, 3904; b) G. Abdelmageed, L. Jewell, K. Hellier, L. Seymour, B. Luo, F. Bridges, J. Z. Zhang, S. Carter, *Appl. Phys. Lett.* **2016**, *109*, 233905.
[35] N. Rai, S. Rai, P. K. Singh, P. Lohia, D. Dwivedi, *J. Mater. Sci.: Mater. Electron.* **2020**, *31*, 16269.
[36] S. Hafiz, F. Zhang, M. Monavarian, V. Avrutin, H. Morkoç, Ü. Özgür, S. Metzner, F. Bertram, J. Christen, B. Gil, *J. Appl. Phys.* **2015**, *117*, 013106.

© 2024 The Authors. Advanced Electronic Materials published by Wiley-VCH GmbH

2199160x, 0, Downloaded from https://onlinelibrary.wiley.com/doi/10.1002/aelm.202400095 by Kumoh National Institute, Wiley Online Library on [12/07/2024]. See the Terms and Conditions (https://onlinelibrary.wiley.com/terms-and-conditions) on Wiley Online Library for rules of use; OA articles are governed by the applicable Creative Commons License

[37] T. Richter, H. L. t. R. Meijers, R. Calarco, M. Marso, *Nano Lett.* **2008**, *8*, 3056.
[38] a) Y. Chang, L. Chen, J. Wang, W. Tian, W. Zhai, B. Wei, *J. Phys. Chem. C* **2019**, *123*, 21244; b) X. Wan, Y. Xu, H. Guo, K. Shehzad, A. Ali, Y. Liu, J. Yang, D. Dai, C.-T. Lin, L. Liu, *Npj 2D Mater. Appl.* **2017**, *1*, 4.
[39] Y. Wang, D. Yang, X. Zhou, S. M. Alshehri, T. Ahamad, A. Vadim, D. Ma, *J. Mater. Chem. C* **2016**, *4*, 7415.
[40] C. H. Kang, G. Liu, C. Lee, O. Alkhazragi, J. M. Wagstaff, K.-H. Li, F. Alhawaj, T. K. Ng, J. S. Speck, S. Nakamura, *Appl. Phys. Express* **2019**, *13*, 014001.
[41] a) V. Mikhelashvili, Y. Shneider, A. Sherman, S. Yofis, G. Ankonina, O. Eyal, I. Khanonkin, G. Eisenstein, *Appl. Phys. Lett.* **2019**, *114*, 073504; b) C. Bao, Z. Chen, Y. Fang, H. Wei, Y. Deng, X. Xiao, L. Li, J. Huang, *Adv. Mater.* **2017**, *29*, 1703209.
[42] L. Al-Maghrabi, C. Huang, D. Priante, M. Tian, J.-W. Min, C. Zhao, H. Zhang, R. C. Subedi, H. H. Alhashim, H. Sun, *AIP Adv.* **2020**, *10*, 055014.
[43] N. Ahn, D.-Y. Son, I.-H. Jang, S. M. Kang, M. Choi, N.-G. Park, *J. Am. Chem. Soc.* **2015**, *137*, 8696.

© 2024 The Authors. Advanced Electronic Materials published by Wiley-VCH GmbH

2199160x, 0, Downloaded from https://onlinelibrary.wiley.com/doi/10.1002/aelm.202400095 by Kumoh National Institute, Wiley Online Library on [12/07/2024]. See the Terms and Conditions (https://onlinelibrary.wiley.com/terms-and-conditions) on Wiley Online Library for rules of use; OA articles are governed by the applicable Creative Commons License